

Advanced Quantum Chemistry Methods - Application Part -

Summer Term 2023

Fabian Herpell

First Submission: 06.07.2023

Contents

1	Electron Correlation	3
1.1	Multireference Methods	3
1.2	Carbenes	5
2	Basis Set Convergence	6
2.1	Formic Acid Dimer	6
3	Thermochemistry	9
3.1	Reaction Enthalpies of Gas-Phase Reactions	9
4	Kinetics	10
4.1	Kinetic Isotope Effect	10
5	Solvation	11
5.1	S _N 2-Reaction	11
6	Activation Energies	12
6.1	Rearrangement and Dimerization Reactions	12
7	Noncovalent Interactions	17
7.1	Noble Gas - Methane	17
8	Spectroscopy	19
8.1	IR-Spectrum of 1,4-Benzoquinone	19
8.2	The Color of Indigo	20
8.3	NMR Parameters	20
9	References	27

1 Electron Correlation

1.1 Multireference Methods

The effect of electron correlation on dissociation curve calculations shall be investigated. Therefore, the potential energy curve of the HF-molecule was computed at the RHF/def2-TZVP, UHF/def2-TZVP, MP2/def2-TZVP, CCSD(T)/def2-TZVP and CASSCF/def2-TZVP (2 and 6 active electrons/orbitals) level of theory.^[1]

To compare the methods, the atom energies were computed for each method (see table 1) and used to calculate potential energy curves relative to them (see figure 1). Since calculating the energy of the hydrogen atom is a one electron problem no electron correlation needs to be considered and all methods except for CCSD(T) yield the same energy.

Table 1: Computed atom energies of H and F at the RHF/def2-TZVP, UHF/def2-TZVP, MP2/def2-TZVP, CCSD(T)/def2-TZVP and CASSCF/def2-TZVP (2 and 6 active electrons/orbitals) level of theory.

Method	E in Hartree	
	H	F
RHF	-0.4998	-99.4118
UHF	-0.4998	-99.4118
MP2	-0.4998	-99.6096
CCSD(T)	-0.4877	-99.6251
CASSCF(2,2)	-0.4998	-99.4072
CASSCF(6,6)	-0.4998	-99.4502

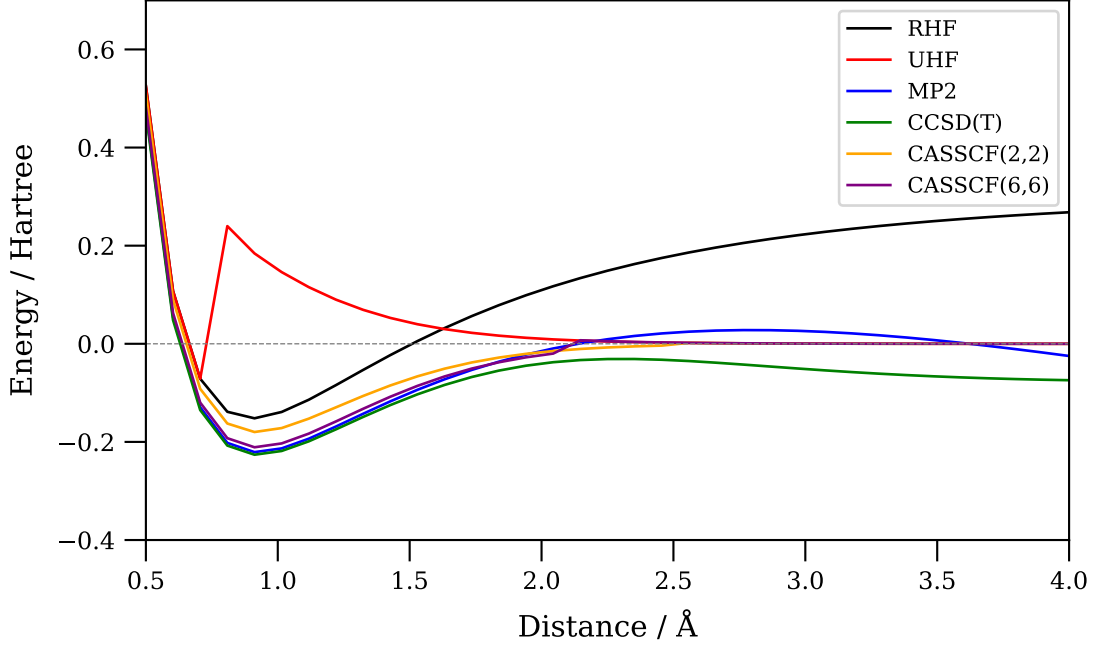


Figure 1: Computed relative potential energy curves of the HF-molecule at the RHF/def2-TZVP, UHF/def2-TZVP, MP2/def2-TZVP, CCSD(T)/def2-TZVP and CASSCF/def2-TZVP (2 and 6 active electrons/orbitals) level of theory.

If we consider CCSD(T) as the method closest to the exact result (for the given basis set), it becomes visible that MP2 and CASSCF(6,6) give almost exact results for the equilibrium. UHF and RHF, on the other hand, overestimate the equilibrium energy. This is explained by the lack of (dynamic) electron correlation in the Hartree Fock procedure. For large distances the RHF Energy increases steadily, which can be explained by the restriction, that both electrons must occupy the same orbital. Therefore, no dissociation is possible. In the UHF case the electrons are allowed to occupy different orbitals, and therefore, UHF describes the correct convergence behaviour for large distances, i.e. convergence to 0. The CASSCF methods include (static) electron correlation, and hence, also show the correct convergence behaviour. The MP2 and CCSD(T) calculations show a steady decrease in energy for large distances. This can be explained by the formula for the correlation energy calculation in the MP2 procedure (see eq. 1), where the HOMO-LUMO gap appears in the nominator. Since the HOMO-LUMO gap converges to zero for large distances (MOs become degenerate) the energy converges to minus infinity for large distances.

$$E^{(2)} = \frac{1}{4} \sum_{n=i,j,a,b} \frac{|\langle ij || ab \rangle|}{\epsilon_i + \epsilon_j - \epsilon_a - \epsilon_b} \quad (1)$$

Since CCSD(T) also includes a MP2 calculation the same behaviour is observed here for large distances.

1.2 Carbenes

In this chapter, the singlet-triplet splitting of methylene and p-benzyne (see figure 2) shall be investigated.

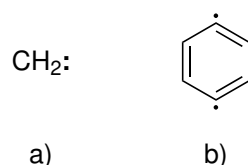


Figure 2: a) Methylene and b) p-Benzyne.

The geometries of the singlet and triplet state were optimized using HF, TPSS, B3LYP, PW6B95 and MP2 with the def2-TZVP basis set.^[1–4] Subsequently, single point energies for all methods were computed. Additionally, the single point energies were calculated for the MP2 optimized geometries at the CCSD(T)/def2-TZVP level of theory. The single point energies were then used to calculate the singlet-triplet splitting (see table 2):

$$\Delta E_{S-T} = E_{\text{singlet}} - E_{\text{triplet}} \quad (2)$$

Table 2: Singlet-triplet splitting of methylene and p-benzyne calculated at the HF, MP2, TPSS, B3LYP and PW6B95 level of theory with a def2-TZVP basis set.

	E / kcal/mol	
	Methylene	p-Benzyne
HF	28.36	80.38
MP2	15.82	-28.55
CCSD(T)	10.78	-3.28
PW6B95	12.57	14.36
TPSS	17.78	7.05
B3LYP	11.91	13.40

The experimentally determined values for the singlet-triplet splittings are 9.0 kcal/mol and -4.2 kcal/mol for methylene and p-benzyne, respectively.^[5] For methylene all methods predict

the qualitatively correct multiplicity, i.e. a triplet state. However, only CCSD(T) comes close to the exact value. For p-benzyne the results are worse: MP2 and CCSD(T) give the correct prediction of a singlet state, whereas all other methods falsely predict a triplet state. Again, the CCSD(T) result is closest to the experimentally determined value. This was to be expected since CCSD(T) is the current "gold standard" of quantumchemical calculations. The extreme failure of HF in both cases can be explained with spin contamination. For the triplet state UHF is needed, which introduces electron correlation (lowers energy) and spin contamination (raises energy).^[6] In total this lowers the energy for the triplet state more than for the singlet state and will therefore falsely stabilise the triplet state compared to the singlet state.

Additionally the bonding angle in methylene was calculated for the triplet and singlet state with the aforementioned methods (see table 3). The experimentally found bonding angles are 102.4° and 135.5° for the singlet and triplet state, respectively.

Table 3: Methylene bonding angles obtained with geometry-optimization using HF, MP2, TPSS, B3LYP and PW6B95 with a def2-TZVP basis set.

	singlet [°]	triplet [°]
HF	103.7500	131.8200
MP2	102.3600	133.0800
TPSS	101.3500	135.3800
B3LYP	101.8700	135.0700
PW6B95	101.6200	134.7800

2 Basis Set Convergence

2.1 Formic Acid Dimer

The basis set (BS) convergence behaviour of the dimerization-energy of formic-acid at the HF-, MP2- and TPSS-D3 level of theory was investigated. Therefore, a geometry optimization of the monomer and dimer was performed at the TPSS-D3/def2-TZVP level of theory and the optimized geometries were used to compute single point energies (HF, MP2, TPSS-D3) with cc-pVXZ and aug-cc-pVXZ basis sets (X = D, T, Q).^[2, 7–9] The dimerization-energies were plotted against the cardinal numbers (X) which is depicted in figure 3, figure 4 and figure 5.

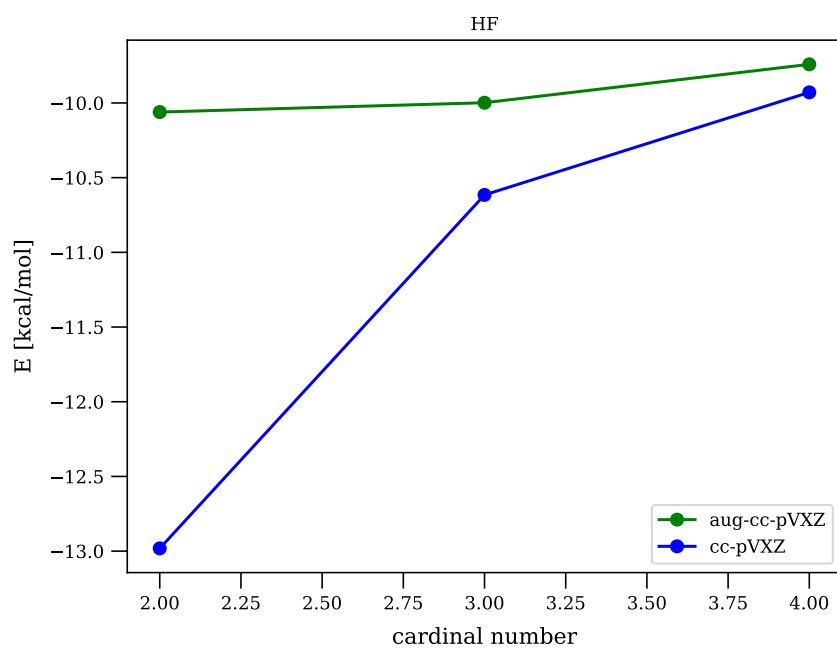


Figure 3: Dimerization-energies calculated at HF-level of theory with cc-pVXZ and aug-cc-pVXZ ($X = D, T, Q$).

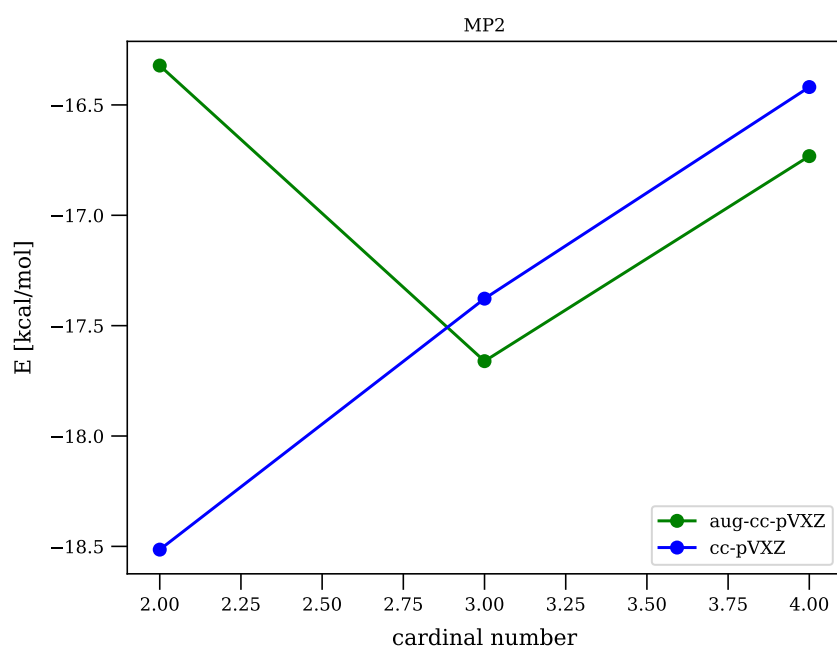


Figure 4: Dimerization-energies calculated at MP2-level of theory with cc-pVXZ and aug-cc-pVXZ ($X = D, T, Q$).

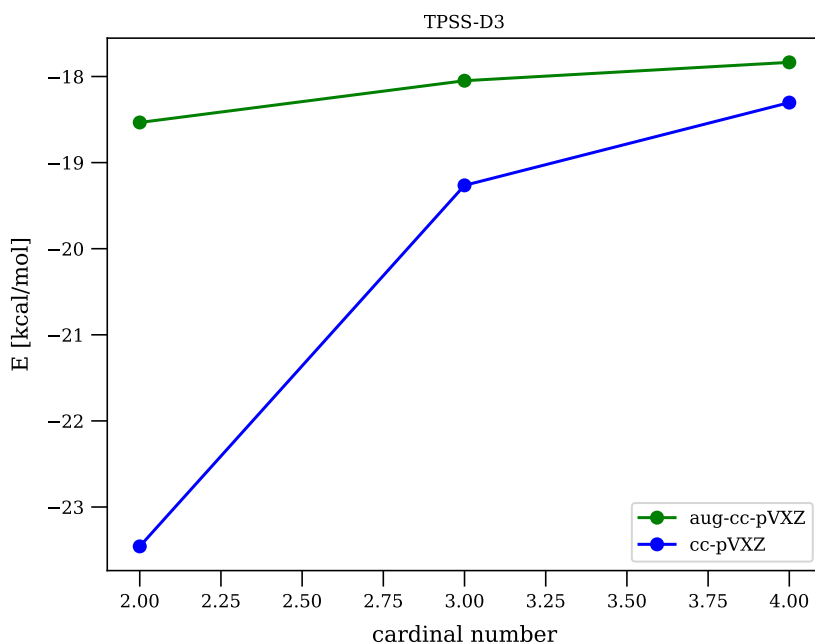


Figure 5: Dimerization-energies calculated at TPSS-D3-level of theory with cc-pVXZ and aug-cc-pVXZ ($X = D, T, Q$).

For all methods and BSs (except MP2/aug-cc-pVDZ) the dimerization-energy converges from an overbinding situation to the CBS limit. This is explained by the BSSE: for the dimer calculation both monomers will have free orbital space left which can be used by the respective other monomer to reduce its BSIE error.^[6] For the calculation of the monomer energies, on the other hand, only the basis set functions assigned to each monomer are available and thus, the BSIE will be higher than for the energy calculation of the dimer. Consequently, the dimerization-energy is artificially lowered.^[6] Increasing the basis set decreases the BSIE and therefore, also the BSSE. Hence, the dimerization-energy increases with higher cardinal numbers.

Comparing the results of aug-cc-pVXZ and cc-pVXZ shows that the augmented BS is higher in energy for a given X (except for MP2). This can be assigned to the decrease of BSIE by adding diffuse function to the cc-pVXZ analogon which leads to an decrease of the BSSE.

Judging by the minor increase of dimerization-energy from the triple- ζ BS to the quadruple- ζ BS in the case of HF and TPSS-D3 calculations, the dimerization-energy can be considered converged for these methods when a quadruple- ζ BS is used.

3 Thermochemistry

3.1 Reaction Enthalpies of Gas-Phase Reactions

The reaction enthalpies ($\Delta_R H$) of the Haber-Bosch (see figure 6 a)) and Steam reforming reaction (see figure 6 b)) were calculated.

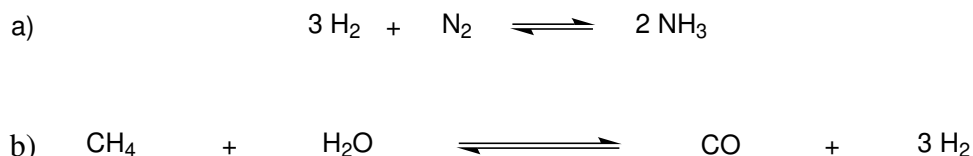


Figure 6: a) Haber-Bosch and b) Steam forming reaction.

Firstly, the atom coordinates of all reactants were optimized at the TPSS-D3/def2-TZVP level of theory.^[2, 7] Subsequently, single point energy calculations of the optimized geometries were performed for all reactants at the TPSS-D3/def2-TZVP, B3LYP-D3/def2-TZVP, MP2/def2-TZVP, B2PLYP-D3/def2-QZVP and CCSD(T)/def2-QZVP level of theory.^[2, 3, 7, 10–12] Additionally enthalpy corrections were calculated for each method and reactant. With these results the reaction enthalpies were calculated using Hess's law. The reaction enthalpies are shown in table 4.

Comparing the results of the calculations to the experimentally found values (Haber-Bosch: -22.5 kcal/mol; Steam reforming: 49.3 kcal/mol)^[5] shows that CCSD(T) and B2-PLYP-D3 give reaction enthalpies within chemical accuracy, B3LYP yields results close to chemical accuracy (for Steam reforming reaction even chemically accurate), and MP2 and TPSS only give qualitatively correct results. This trend is as expected since TPSS as a meta GGA is on the Jacob's ladder below the hybrid functional B3LYP and the double hybrid functional B2-PLYP. As CCSD(T) is the current "gold standard" of quantum chemistry calculations its results are expected to be the most accurate. However, it only yields the smallest deviation from the experimental value for the Haber-Bosch reaction. Surprisingly, the B2-PLYP calculation outperforms the CCSD(T) calculation in case of the steam reforming reaction with the same basis set.

Table 4: Reaction enthalpies of the Haber-Bosch and Steam reforming reaction calculated using TPSS-D3/def2-TZVP, B3LYP-D3/def2-TZVP, MP2/def2-TZVP, B2-PLYP-D3/def2-QZVP and CCSD(T)/def2-QZVP.

	$\Delta_R H$ [kcal/mol]	
	Haber-Bosch	Steam reforming
MP2	-10.5	41.8
CCSD(T)	-22.8	50.0
TPSS	-12.7	42.4
B3LYP	-20.8	47.3
B2-PLYP	-22.9	49.7
experimental value	-22.5	49.3

Additionally, the geometry optimizations of the Haber-Bosch reactants were done at the MP2/def2-TZVP level of theory to calculate the root mean square deviation (RMSD) with respect to the optimized geometries using TPSS-D3/def2-TZVP. As can be seen in table 5 the RMSD is small and consequently geometry optimization is rather insensitive to the chosen method (at least for this example). Hence, using a computationally cheap method is reasonable to obtain the optimized geometries.

Table 5: Root mean square deviation (RMSD) of the geometry optimized coordinates calculated with MP2/def2-TZVP and TPSS-D3/def2-TZVP.

	NH ₃	N ₂	H ₂
RMSD	0.006569	0.005674	0.003063

4 Kinetics

4.1 Kinetic Isotope Effect

The kinetic isotopic effect has been investigated for the reaction of CH₄ (see figure 7 a)) and CD₄ (see figure 7 b)) with the hydroxy radical.

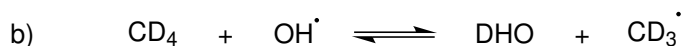
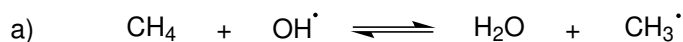


Figure 7: a) Hydrogen- and b) deuterium atom transfer reaction to hydroxy radical.

To do this all geometries were set up using chemical intuition and subsequently energy calculations of the reactants as well as a transition state (TS) search were performed on the B3LYP-D3/def2-TZVP level of theory.^[1, 3, 7] The TSs were validated by the fact that only one imaginary frequency was present. In addition, the thermal enthalpy corrections were calculated for the reactants and the TSs. With these results the activation enthalpies (ΔH^\ddagger) were calculated as follows:

$$\Delta H^\ddagger = H_{\text{TS}} - H_{\text{starting structure}} \quad (3)$$

The ΔH^\ddagger for the hydrogen atom- and deuterium atom transfer are -0.66 kcal/mol and 0.45 kcal/mol, respectively. From these values the quotient of both rate constants k_H/k_D can be calculated:

$$k_H/k_D = \exp(-(\Delta H_H^\ddagger - \Delta H_D^\ddagger)/RT) = 6.46 \quad (4)$$

The atom transfer will be roughly 6.5 times faster for deuterium than for hydrogen at equal concentrations. Since the difference between deuterium and hydrogen is one neutron, the electronic energy, which only depends on the number of electrons and protons as well as their positions, for both reactions is identical. Consequently, the thermal corrections are responsible for the nonidentical rate constants.

5 Solvation

5.1 S_N2 -Reaction

To investigate the solvation effect, the potential energy curve of the S_N2 -reaction of methylchloride (MeCl) with fluoride (see figure 8) was calculated in the gas phase and in MeOH.



Figure 8: S_N2 -Reaction of MeCl with fluoride.

The potential energy curves were calculated by performing geometry optimizations at carbon-fluor distances of 2.25 bohr (a_0) to 8.00 a_0 in steps of 0.25 a_0 at the PW6B95-D3/def2-TZVP level of theory.^[1, 4, 7] Using the COSMO-approach, MeOH is simulated with a dielectric constant of $\epsilon = 32.0$.^[13] The potential energy curves (see figure 9) show a (local) minimum in energy at 2.75 a_0 (MeF equilibrium distance) and a (local) maximum in energy around 4 a_0 (TS). For smaller C-F distances than 2.75 a_0 the nuclear-nuclear repulsion overrules the energy

gain due to increasing orbital overlap, and hence, the energy increases. For large C-F distances the energy for the calculation in MeOH converges to 0 kcal/mol, whereas in the gas phase a steady energy increase is observed. This can be explained due to missing stabilization of the negative charge at the free fluoride ion in the gas phase which is stabilized due to solvation in the case of the calculation in MeOH.

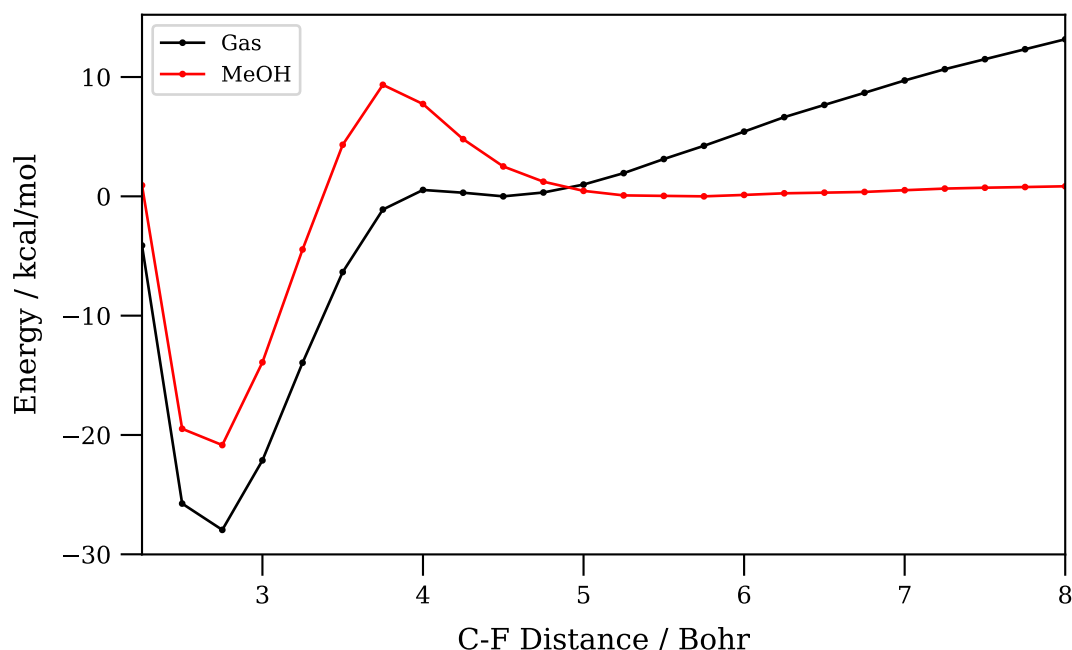


Figure 9: Potential energy curves (lowest energy of starting material set to 0) of the S_N2 -Reaction of MeCl with fluoride in the gas phase and in MeOH.

Additionally, the activation barriers can be estimated from figure 9 by calculating the free activation Enthalpies ΔG^\ddagger : $\Delta G^\ddagger_{\text{gas}} = 0.54$ kcal/mol and $\Delta G^\ddagger_{\text{MeOH}} = 9.35$ kcal/mol. The roughly 17 times smaller activation energy in the gas phase stems from the prior discussed higher energy of the fluoride ion in the gas phase compared to the solvated ion and explicitly not from the (minor) more stable TS.

6 Activation Energies

6.1 Rearrangement and Dimerization Reactions

The activation energy of a Diels-Alder- (see figure 10 a)) and a Claisen-reaction (see figure 10 b)) were calculated.

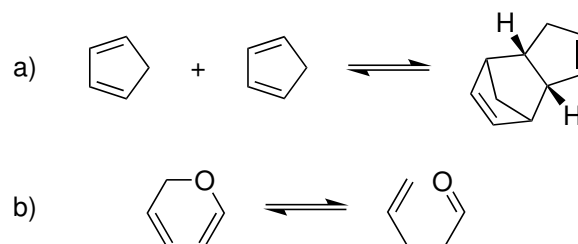


Figure 10: a) Diels-Alder reaction (endo product) and b) Claisen rearrangement.

To find a transition state (TS), the geometries of all reactants were optimized using the GFN2-xTB method.^[14] The obtained geometries were used for a subsequent transition state search with orca. The calculated relative energy with respect to the reaction coordinate is depicted in figure 11 (Diels-Alder) and figure 12 (Claisen).

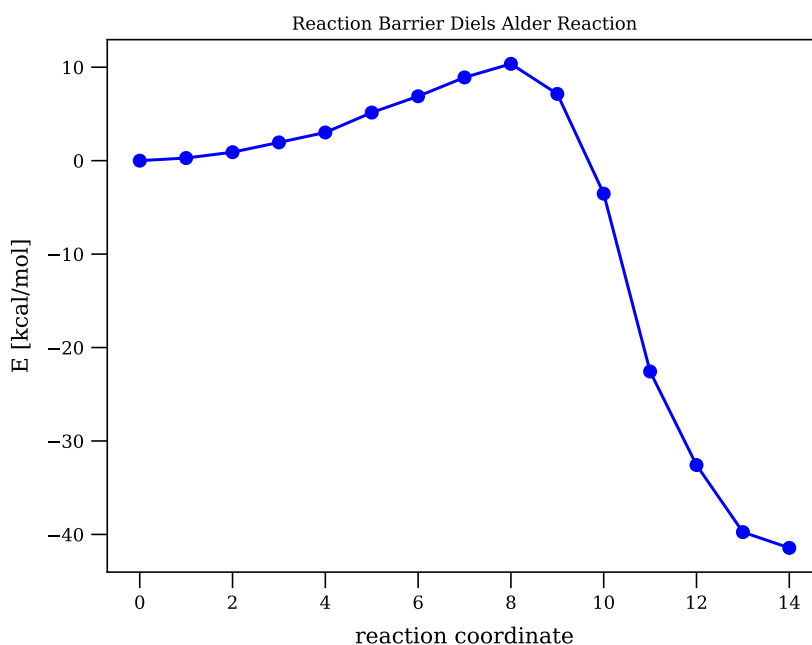


Figure 11: Reaction Barrier of the Diels-Alder reaction (calculated with GFN2-xTB).

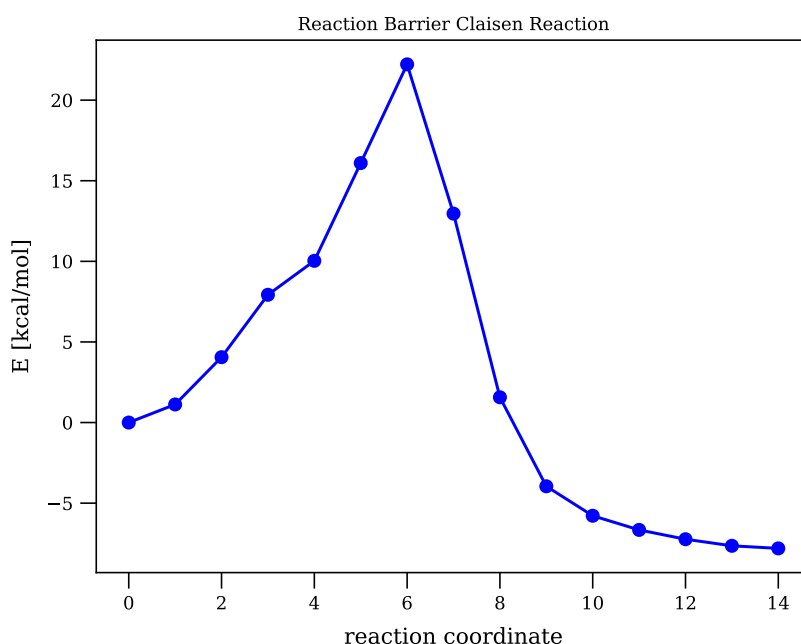


Figure 12: Reaction Barrier of the Claisen reaction (calculated with GFN2-xTB).

The activation energy (ΔG^\ddagger) can be directly obtained from figure 11 and figure 12

$$\Delta G_{\text{Diels-Alder}}^\ddagger = 10.4 \text{ kcal/mol}$$

$$\Delta G_{\text{Claisen}}^\ddagger = 22.2 \text{ kcal/mol}$$

Additionally, the activation energy for both reactions has been calculated by doing single point energy calculations on the geometry optimized starting structures and the transition states at the PW6B95-D3/def2-TZVP level of theory. The ΔG^\ddagger was then calculated as follows:

$$\Delta G^\ddagger = G_{\text{TS}} - G_{\text{starting structure}} \quad (5)$$

The resulting activation energies were determined to be $\Delta G_{\text{Diels-Alder}}^\ddagger = 17.0 \text{ kcal/mol}$ and $\Delta G_{\text{Claisen}}^\ddagger = 36.9 \text{ kcal/mol}$. The calculations using the GFN2-xTB method yield lower activation energies (roughly a factor of 1/2 smaller) than the PW6B95-D3/def2-TZVP calculations. This can be designated to the fact that HF exchange is included in the hybrid functional PW6B95^[15], whereas the GFN2-xTB method is free of HF (Hartree Fock) exchange^[14]. HF is known to overestimate reaction barriers^[16].

Furthermore, the TSs are depicted in figure 13 (Diels-Alder) and 14 (Claisen) with the most important bond distances highlighted.

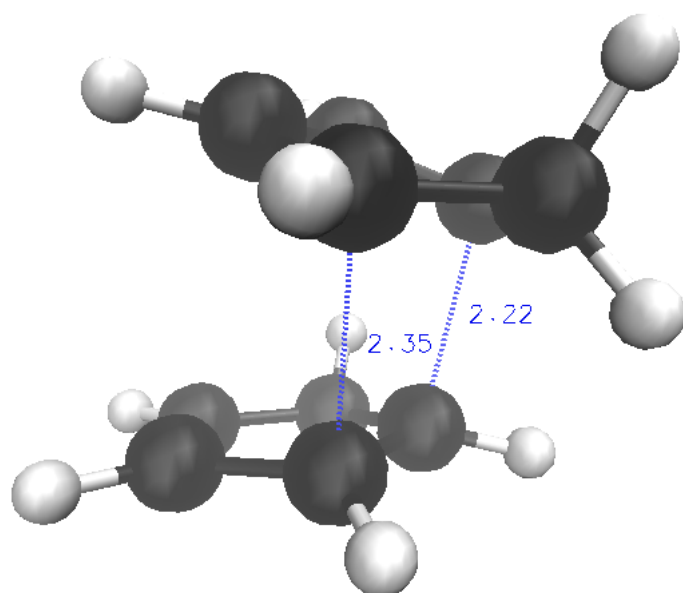


Figure 13: TS of the Diels-Alder reaction.

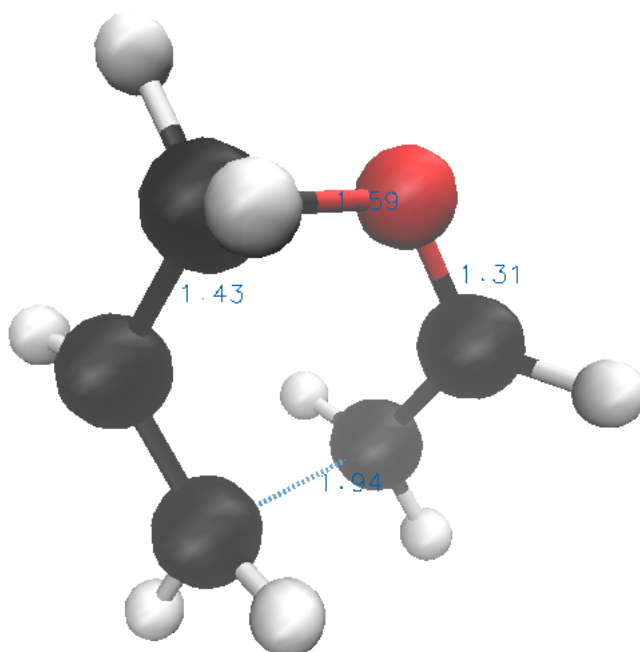


Figure 14: TS of the Claisen reaction.

For the TS of the Claisen reaction (figure 14) four bond distances are highlighted to illustrate the bond order changes during the reaction. The bond distance between the carbon atom and oxygen atom which are forming a double bond is with 1.31 Å smaller than for a C-O single bond (1.43 Å^[17]), however, still larger than for a C=O bond (1.19 Å^[17]). The bond distance between the oxygen atom and carbon atom where the C-O bond is breaking is with 1.59 Å smaller than a C-O single bond distance. Furthermore, the C-C distance between the carbon atoms which end up double bonded is with 1.43 Å smaller than for a C-C single bond (1.54 Å^[17]). Lastly, the carbon atoms which form a new C-C bond have a distance of 1.94 Å. To improve the results one could do the single point energy calculations on a higher level of theory than PW6B95-D3/def2-TZVP. Since PW6B95 is a hybrid meta GGA^[15] a double

hybrid functional or a CCSD(T) calculation should improve the results. Furthermore, the geometry optimization at a higher level of theory than GFN2-xTB seems feasible considering the relative small size of the systems. Applying higher level of theories, however, will increase computational time which will limit the approach to small systems.

7 Noncovalent Interactions

7.1 Noble Gas - Methane

The noncovalent interaction energy between methane (CH_4) and Ar as well as between CH_4 and Kr shall be investigated. Therefore, geometry optimizations for C-X ($X = \text{Ar}, \text{Kr}$) distances from $4.5 a_0$ to $15.0 a_0$ in $0.25 a_0$ steps were calculated using the BLYP/def2-QZVP, BLYP-D3/def2-QZVP and MP2/def2-QZVP method.^[1, 3, 7, 10] The results can be seen in figure 15 and figure 16 for the $(\text{CH}_4)\text{-Ar}$ and the $(\text{CH}_4)\text{-Kr}$ dimer, respectively.

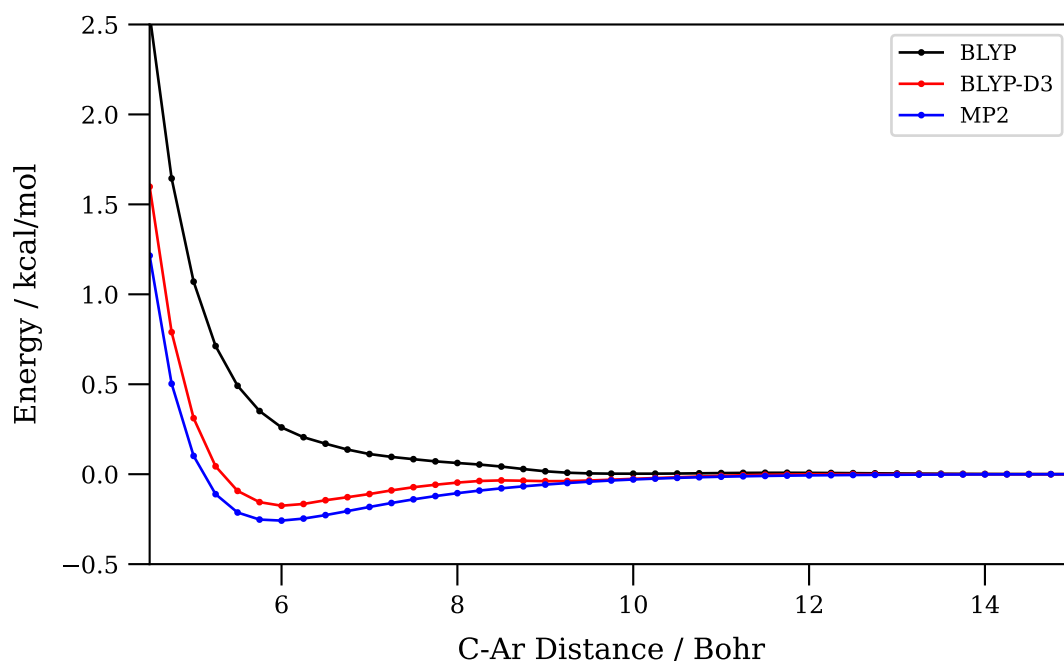


Figure 15: Potential energy curves of the $\text{CH}_4\text{-Ar}$ Dimer calculated at BLYP/def2-QZVP, BLYP-D3/def2-QZVP and MP2/def2-QZVP level of theory.

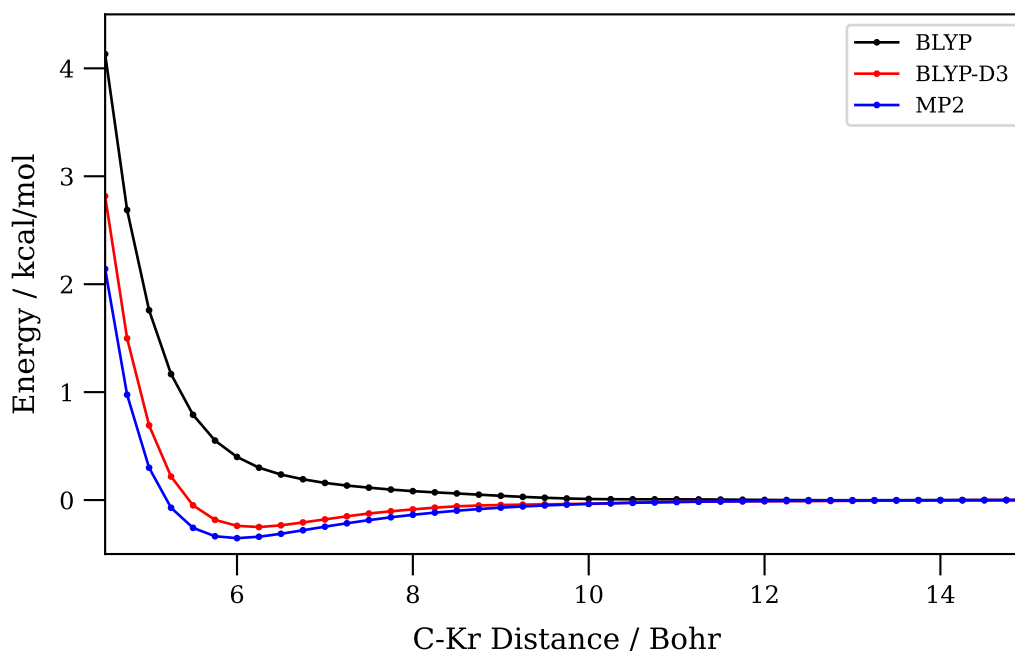


Figure 16: Potential energy curves of the $\text{CH}_4\text{-Kr}$ Dimer calculated at BLYP/def2-QZVP, BLYP-D3/def2-QZVP and MP2/def2-QZVP level of theory..

Considering all three methods, only BLYP-D3 and MP2 give a qualitatively correct result, i.e. a negative dimerization energy. Since BLYP as a meta GGA has no long-range correlation included, which are needed for dispersion energy calculation, it fails to find a minimum unless the dispersion correction (D-3) is added.^[18] MP2, on the other hand, includes dispersion energy intrinsically due to included virtual orbitals. For the $\text{CH}_4\text{-Ar}$ dimer BLYP-D3 and MP2 find the same equilibrium distance ($6.0 a_0$) and for the $\text{CH}_4\text{-Kr}$ dimer the equilibrium distance calculated with MP2 ($6.0 a_0$) is just slightly smaller than the one calculated with BLYP-D3 ($6.25 a_0$). Overall, the potential energy curves of both dimers look quite similar, except for small distances. Here, the $\text{CH}_4\text{-Kr}$ dimer shows higher repulsion than the $\text{CH}_4\text{-Ar}$ dimer. This can be designated to the fact, that Kr has more electrons than Ar which consequently leads to higher pauli-repulsion with CH_4 .

8 Spectroscopy

8.1 IR-Spectrum of 1,4-Benzoquinone

In this chapter the IR-spectrum of 1,4-benzoquinone (see figure 17) is investigated.

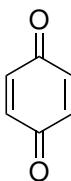


Figure 17: 1,4-Benzoquinone.

To calculate the IR-spectrum, the geometry of 1,4-benzoquinone was optimized at the HF-D3/def2-SVP and TPSS-D3/def2-SVP level of theory.^[1, 2, 7] Subsequently, the normal modes were calculated. To compare the energies of the normal modes to the experimentally found IR-spectrum^[19], the scaling factor (f_{scal}) for the computed wavenumbers was calculated as follows:

$$f_{\text{scal}} = \frac{\nu_{\text{comp.}}}{\nu_{\text{exp}}} \quad (6)$$

The results are depicted in table 6.

Table 6: Calculated frequencies of 1,4-benzoquinone normal modes compared to a measured IR-spectrum.

Experiment	HF-D3		TPSS-D3	
$\nu_{\text{exp}} / \text{cm}^{-1}$	$\nu_{\text{HF-D3}} / \text{cm}^{-1}$	f_{scal}	$\nu_{\text{TPSS-D3}} / \text{cm}^{-1}$	f_{scal}
880	988.5	0.89	902.3	0.98
1050	1167.3	0.90	1057.0	0.99
1300	1452.2	0.90	1297.4	1.00
1600	1861.2	0.86	1616.7	0.99
1675	2028.6	0.83	1700.2	0.99

In addition, the mean scaling factors for both methods were calculated to compare their overall accuracy: $f_{\text{scal}}^{\text{HF-D3}} = 0.88$, $f_{\text{scal}}^{\text{TPSS-D3}} = 0.99$. The TPSS-D3 calculations are very close to the experimentally obtained wavenumbers, whereas HF-D3 calculation are inherently too large. The latter is a consequence of the too short bond lengths yielded by HF calculations.

8.2 The Color of Indigo

In the following, TD-HF (time dependent HF) and TD-DFT (time dependent DFT) calculations will be used to predict the color of indigo (see figure 18).

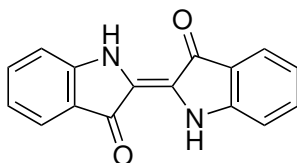


Figure 18: Indigo.

Firstly, the geometry of indigo was optimized at the TPSS-D3/def2-SVP level of theory.^[1, 2, 7] Secondly, single point calculations were performed at the HF-D3/def2-SVP, PBE-D3/def2-SVP and PBE0-D3/def2-SVP level of theory.^[1, 7, 20, 21] Eventually, the TD-HF/DFT calculations were carried out. From the computed excitation energies the color of indigo can be predicted as the complementary color, which is depicted in figure 7.

Table 7: Calculated excitation energies at the HF-D3/def2-SVP, PBE-D3/def2-SVP and PBE0-D3/def2-SVP level of theory and the resulting color prediction for indigo.

Method	E / Hartree	E / eV	ν / cm^{-1}	λ / nm	color
HF-D3	0.1216	3.3097	26694	374.6	green
PBE-D3	0.0738	2.0072	16189	617.7	blue
PBE0-D3	0.0855	2.3253	18755	533.2	purple

Only the PBE-D3 calculation gives a qualitatively correct result, i.e. a prediction of blue color. HF-D3 and PBE0-D3 overestimate the excitation energies. Considering Jacob's ladder, it is surprising that the hybrid variant of PBE gives a worse result than PBE itself. However, it can be seen that HF-D3 gives even worse results with the used small BS (def2-SVP). Since the exchange Energy of HF is also mixed into PBE0, the overestimation of the excitation energy might also be introduced. Using a larger BS should correct for that problem.

8.3 NMR Parameters

In this chapter ^{13}C -NMR parameters for small organic substances (see figure 19 **A-G**) and aromatic systems (see figure 19 **Ar-1-Ar-4**) as well as ^1H -NMR parameters for methine protons in two medium sized molecules (see figure 19 **H, I**) shall be calculated. Furthermore, the influence of solvation to NMR-parameters will be investigated.

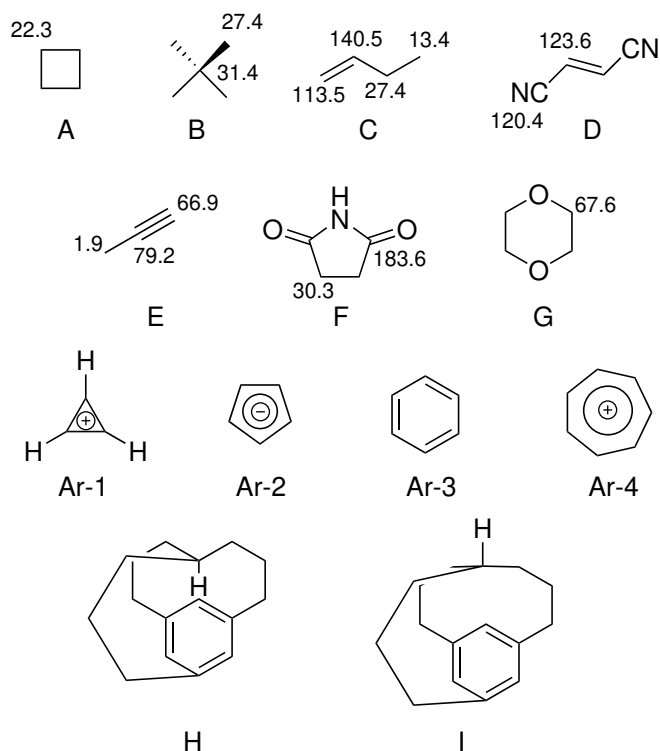


Figure 19: Investigated structures and their measured ^{13}C -NMR signals.^[5]

Firstly, all structure were optimized at the PBEh-3c level of theory.^[22] Afterwards, isotropic NMR shielding constants (σ) were calculated at the PBE/pcSseg-2 level of theory.^[20, 23] References were calculated in the same manner to obtain chemical shifts (δ):

$$\delta_c = \sigma_{ref} - \sigma_c \quad (7)$$

For ^{13}C -NMR and ^1H -NMR Tetramethylsilane (TMS) was used as a reference, which has the following isotropic shielding constants:

$$\sigma_{TMS,C} = 181.7 \text{ ppm}$$

$$\sigma_{TMS,H} = 31.5 \text{ ppm}$$

In table 8 the calculated chemical shifts of **A-G** and their deviation to the experiment are depicted.

Table 8: Calculated chemical shifts of **A-G** and their deviation to the experiment.

Molecule	σ_{calc} / ppm	δ_{calc} / ppm	δ_{exp} / ppm	$\Delta\delta$ / ppm
A	154.7	27.0	22.3	4.7
B	147.9	33.9	31.4	2.5
	147.4	34.4	27.4	7.0
C	59.9	121.8	113.5	8.3
	26.2	155.5	140.5	15.0
	145.2	36.5	27.4	9.1
	164.4	17.3	13.4	3.9
D	57.8	124.0	120.4	3.6
	53.8	128.0	123.6	4.4
E	110.5	71.2	66.9	4.3
	96.4	85.3	79.2	6.1
	177.7	4.0	1.9	2.1
F	-0.5	182.2	183.6	-1.4
	147.8	33.9	30.3	3.6
G	107.2	74.5	67.6	6.9

To evaluate the accuracy of the computed chemical shifts, the mean deviation (MD) and mean absolute deviation (MAD) are useful values:

$$MD = \sum_{i=1}^N (\delta_{\text{calc}} - \delta_{\text{ref}}) \quad (8)$$

$$MAD = \sum_{i=1}^N |\delta_{\text{calc}} - \delta_{\text{ref}}| \quad (9)$$

For the ^{13}C -NMR of **A-G** they are: MD = 5.3 ppm and MAD = 5.5 ppm. This shows, that on average all ^{13}C -NMR chemical shifts are overestimated, which is true for all chemical shifts except of one of compound **F**. The latter outlier is the reason why the MAD is slightly larger than the MD.

Additionally, the ^{13}C -NMR chemical shifts of four aromatic systems (see figure 19 **Ar-1-Ar-4**) were computed with the method discussed above. The results can be seen in table 9.

Table 9: Calculated ^{13}C -NMR chemical shifts of **Ar-1-Ar-4**.

Molecule	σ_{calc} / ppm	δ_{calc} / ppm
Ar-1	- 4.8	186.5
Ar-2	77.3	104.4
Ar-3	45.2	136.6
Ar-4	16.9	164.8

To rationalize the results in table 9 with respect to the π -electron density (ρ_{π}), the chemical shifts are plotted against ρ_{π} (figure 20). ρ_{π} is calculated as follows (n_{el}^{π} = number of π -electrons, n_{at}^{π} = number of atoms that contribute to n_{el}^{π}):

$$\rho_{\pi} = \frac{n_{el}^{\pi}}{n_{at}^{\pi}} \quad (10)$$

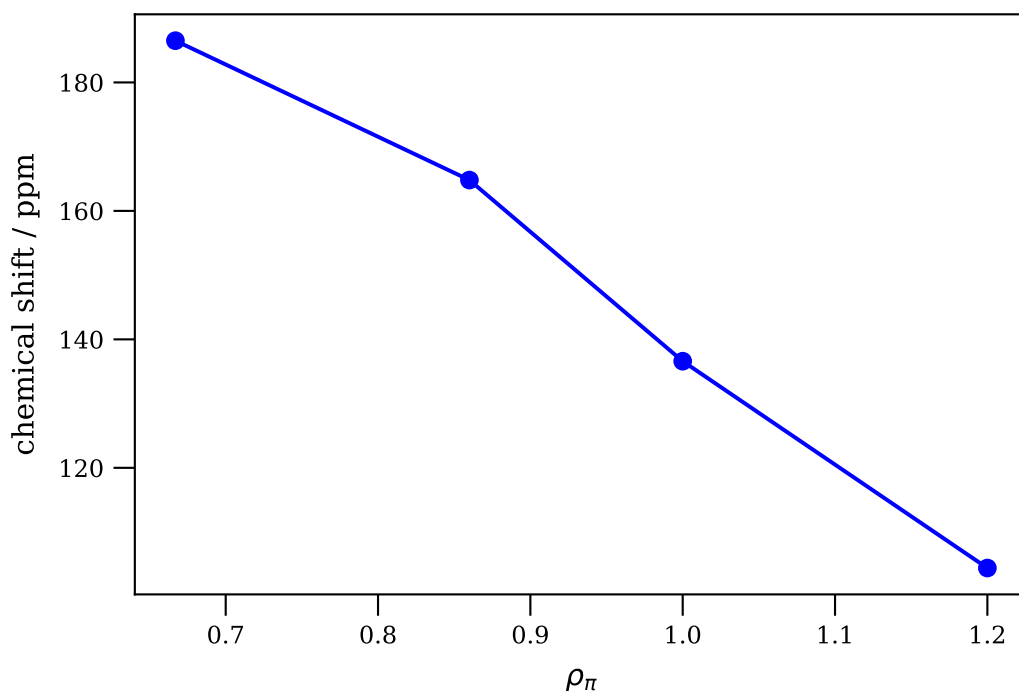


Figure 20: Plot of σ against π -electron-density for **Ar-1-Ar-4**.

The chemical shifts show an almost linear decrease for increasing π -electron density. This is reasonable, since a higher electron density around the nucleus will weaken the local magnetic field during NMR measurement, and therefore, decrease the splitting of nuclear spin states

(equal to decreasing chemical shift).

In addition, the ^1H -NMR chemical shift of the methine protons in **H** and **I** were calculated with the above described method using TMS as reference. The results can be seen in table 10. As expected, the methine proton facing towards the aromatic ring (**H**) has a lower chemical shift than the methine proton pointing away from the aromatic ring (**I**). This can be explained by the aromatic-ring-current, which will decrease the local magnetic field for nuclei above the aromatic system. Since in **I** the proton points away from the aromatic system the shielding is smaller than for **H**, where the proton is right above the aromatic system.

Table 10: Calculated ^1H -NMR chemical shifts of the methine proton of **H** and **I**.

Molecule	$\sigma_{\text{calc}} / \text{ppm}$	$\delta_{\text{calc}} / \text{ppm}$
H	34.7	-3.2
I	29.4	2.1

Last but not least, the effect of solvation and geometry optimization shall be investigated. Therefore, the ^{13}C -NMR chemical shieldings and ^{17}O -NMR chemical shieldings of the carbonyl group of acetone were calculated four times (level of theory identical to prior NMR-calculations/geometry optimizations in this chapter): geometry optimization in the gas phase and NMR-calculation in the gas phase (GG), geometry optimization in water and NMR-calculation in water (WW), geometry optimization in the gas phase and NMR-calculation in water (GW), and geometry optimization in water and NMR-calculation in the gas phase (WG). The calculations in water were done using the implicit solvent model CPCM.^[13] The reference for the ^{13}C -NMR chemical shifts is TMS and for the ^{17}O -NMR chemical shifts is water. The reference NMR-data was calculated in the same manner as the NMR-data for acetone. The results for the references are shown in table 11 (^{13}C -NMR) and table 12 (^{17}O -NMR)

Table 11: ^{13}C -NMR chemical shieldings of TMS.

Optimization/NMR-Calculation	$\sigma_{\text{calc}} / \text{ppm}$
GG	181.7
WW	182.7
WG	181.5
GW	182.9

Table 12: ^{17}O -NMR chemical shieldings of water.

Optimization/NMR-Calculation	σ_{calc} / ppm
GG	330.5
WW	338.4
WG	329.2
GW	339.4

With the references in hand, the chemical shifts of the carbonyl group of acetone for all four calculations were obtained (see eq. 7). The results are depicted in table 13. It can be seen that the chemical shift calculations are rather insensitive to the use of solvation effects during geometry optimization (GG and WG / WW and GW give similar values), whereas the the solvation effects during the NMR-calculations have a pronounced effect (GG and GW / WW and WG have relatively large deviations).

Table 13: Calculated ^{13}C - / ^{17}O -NMR chemical shieldings and shifts of the carbonyl function of acetone for GG, WW, WG and GW.

Geo. Opt./NMR-Calc.	^{13}C		^{17}O	
	σ_{calc} / ppm	δ_{calc} / ppm	σ_{calc} / ppm	δ_{calc} / ppm
GG	-34.8	216.5	-339.2	669.7
WW	-47.6	230.3	-286.4	624.8
WG	-37.3	218.8	-349.1	678.3
GW	-44.9	227.8	-279.8	619.2

Furthermore, the shift of the chemical shift ($\Delta\delta$) of the ^{13}C - and ^{17}O -NMR can be evaluated as the difference between the chemical shift calculated in gas and water (see table 14).

Table 14: Calculated $\Delta\delta$ of the ^{13}C - and ^{17}O -NMR chemical shifts of acetone between being in the gas phase and water.

Optimization/NMR-Calculation	$\Delta\delta$ / ppm	
	^{13}C	^{17}O
GG - GW	-11.3	50.5
WG - WW	-11.5	53.5
GG - WW	-13.8	44.9

The experimentally found $\Delta\delta$ are: $\Delta\delta_{^{13}\text{C}} = -18.9$ ppm and $\Delta\delta_{^{17}\text{O}} = 75.5$ ppm.^[5] The calculated

values are qualitatively correct.

9 References

- [1] F. Weigend, R. Ahlrichs, *Physical Chemistry Chemical Physics* **2005**, 7, 3297–3305.
- [2] J. Tao, J. P. Perdew, V. N. Staroverov, G. E. Scuseria, *Physical review letters* **2003**, 91, 146401.
- [3] A. D. Becke, *The Journal of Chemical Physics* **1993**, 98, 5648–5652.
- [4] Y. Zhao, D. G. Truhlar, *The Journal of Physical Chemistry A* **2005**, 109, 5656–5667.
- [5] Grimme Group, QC2-Advanced Quantum Chemistry Methods, **2023**.
- [6] F. Jensen, *Introduction to computational chemistry*, John wiley & sons, **2017**.
- [7] S. Grimme, J. Antony, S. Ehrlich, H. Krieg, *The Journal of chemical physics* **2010**, 132, 154104.
- [8] T. H. Dunning Jr, *The Journal of chemical physics* **1989**, 90, 1007–1023.
- [9] R. A. Kendall, T. H. Dunning Jr, R. J. Harrison, *The Journal of chemical physics* **1992**, 96, 6796–6806.
- [10] C. Møller, M. S. Plesset, *Phys. Rev.* **1934**, 46, 618–622.
- [11] S. Grimme, *The Journal of chemical physics* **2006**, 124, 034108.
- [12] K. Raghavachari, G. W. Trucks, J. A. Pople, M. Head-Gordon, *Chemical Physics Letters* **1989**, 157, 479–483.
- [13] A. Klamt, G. Schüürmann, *Journal of the Chemical Society Perkin Transactions 2* **1993**, 799–805.
- [14] C. Bannwarth, S. Ehlert, S. Grimme, *Journal of chemical theory and computation* **2019**, 15, 1652–1671.
- [15] Y. Zhao, D. G. Truhlar, *The Journal of Physical Chemistry A* **2005**, 109, 5656–5667.
- [16] S. Grimme, Quantum Chemistry I - Lecture, **Winter term 2022/23**.
- [17] A. Holleman, E. Wiberg, N. Wiberg, 102. Auflage, Lehrbuch der anorganischen Chemie, **2007**.
- [18] G. A. DiLabio, A. Otero-de-la-Roza, *Reviews in computational chemistry* **2016**, 29, 1–97.
- [19] <https://webbook.nist.gov/cgi/cbook.cgi?Name=1%2C4-benzoquinoneUnits=SI>; last visit: 02.07.2023.
- [20] J. P. Perdew, K. Burke, M. Ernzerhof, *Physical review letters* **1996**, 77, 3865.

- [21] C. Adamo, V. Barone, *The Journal of chemical physics* **1999**, *110*, 6158–6170.
- [22] S. Grimme, J. G. Brandenburg, C. Bannwarth, A. Hansen, *The Journal of chemical physics* **2015**, *143*.
- [23] F. Jensen, *Journal of Chemical Theory and Computation* **2015**, *11*, 132–138.